Mechanical Systems and Signal Processing 195 (2023) 110242

Contents lists available at ScienceDirect

Mechanical Systems and Signal Processing

journal homepage: www.elsevier.com/locate/ymssp

A novel robust edge detection method for full-field modal parameter estimation using an image-based tracking continuously scanning laser Doppler vibrometer system

L.F. Lyu, G.D. Higgins, W.D. Zhu *

Department of Mechanical Engineering, University of Maryland, Baltimore County, 1000 Hilltop Circle, Baltimore, MD 21250, USA

ARTICLE INFO

Keywords:
Robust edge detection method
image-based tracking continuously scanning
laser Doppler vibrometer system
Two-dimensional scan
Improved demodulation method
Operational modal analysis

ABSTRACT

A novel robust edge detection method is developed for an image-based tracking continuously scanning laser Doppler vibrometer (CSLDV) system to track a rotating structure without attaching any encoder or mark to it and scan its whole surface. The robust edge detection method can extract edges of the rotating structure from its complex background by processing grayscale images of the rotating structure. Once edges of the rotating structure are clearly shown in the processed image, their positions can be easily determined. To track a rotating structure like a rotating blade of a wind turbine with multiple blades, a distance condition is used to determine the position of an edge of the structure that needs to be tracked and estimate its real-time rotation speed. Once the position of the edge of the rotating structure is determined, the image-based tracking CSLDV system can scan the whole surface of the rotating structure via a two-dimensional scan scheme. An improved demodulation method is used to process measured data of response of the rotating structure subject to random excitation and estimate its modal parameters including damped natural frequencies and full-field undamped mode shapes. The robust edge detection method is investigated by tracking and scanning a rotating fan blade subject to random excitation with a complex background using the image-based tracking CSLDV system, and estimating modal parameters of the rotating fan blade with different constant speeds.

1. Introduction

Global wind power capacity has continued to grow rapidly over the past few decades. In 2020, the newly installed capacity of global wind power reached a record of nearly 93 GW, and the cumulative installed capacity of global wind power was 743 GW [1]. Most of installed wind turbines are aging, which is driving the growth of the operation and maintenance (O&M) market of wind power and the need for advanced repair techniques of wind turbines [2]. The global O&M market of wind power was expected to reach $27.4 billion by 2025 at a compound annual growth rate of 8% [3]. Blades are the fifth largest contributors of overall wind turbine failures, accounting for 6.2% of overall wind turbine failures [4]. Among all components of wind turbines, blades, as well as hubs and gear boxes, require longest repair times, highest repair costs, and largest numbers of technicians for repair [4]. Wind turbine blades should be monitored under operational conditions to detect potential damages that may cause sudden failures of wind turbines. Visual inspection is the primary means of vibration monitoring and structural health monitoring (SHM) of stationary wind turbine blades,

* Corresponding author.
E-mail address: wzhu@umbc.edu (W.D. Zhu).

https://doi.org/10.1016/j.ymssp.2023.110242
Received 7 November 2022; Received in revised form 24 January 2023; Accepted 25 February 2023
Available online 24 March 2023

which can take 1–3 days and cost up to €10,000 for one wind turbine per year [2,4]. An efficient and low-cost non-contact method is urgently needed for monitoring vibrations of wind turbine blades under operational conditions.

The key of contactless vibration monitoring and SHM of a rotating structure like a rotating wind turbine blade is to determine its position at any time instant. Image-based methods, such as edge detection methods, are suitable for determining the position of a moving object without attaching any sensor to it. An edge detection method converts a digital image to a binary image by locating discontinuities of image brightness, and these discontinuities may correspond to edges of the object in the image [5]. An edge detection method basically consists of filtering, enhancement, detection, and localization [6]. Filtering is removing ambient noise in an image while keeping all strong edges clear in the image. Enhancement is emphasizing regions where pixel intensity varies significantly to aid gradient computation. Detection is removing false edges due to noise while preserving pixels that make up true edges in the image. Localization is obtaining exact locations of edges in the image [6–8]. Edge detection methods have been used for motion tracking [9–14]. An edge detection method was developed for tracking the moving path of an object in Ref. [9]. Laurence [10] compared motion tracking of a rigid body using an edge detection method and the least square fitting method. Li et al. [11] developed a rotation feature extraction method for determining the rotation rate and radius of a moving object based on a temporal differencing method and an image edge detection method. Zhao et al. [12] combined a structural sparse representation method, a semi-supervised learning method, and an edge detection method for tracking a moving object. Bai et al. [13] developed a method for monitoring the displacement of a structure based on an edge detection method. Daga and Garibaldi [14] developed an adaptive template matching method based on a genetic algorithm method and an edge detection method for determining the instantaneous rotation speed of a structure. These methods were developed only for determining positions of a moving structure, and have not been applied to vibration monitoring and SHM of a rotating structure.

To measure the vibration of a rotation structure without contact, one can combine an edge detection method and a noncontact vibration measurement method. A laser Doppler vibrometer is a suitable noncontact method for vibration monitoring and SHM of a structure since it accurately measures the structural surface velocity of a point [15,16]. A continuously scanning laser Doppler vibrometer (CSLDV) system that could sweep its laser spot on a prescribed scan path was developed to measure the vibration on the scan path [17–20]. Measurement of the CSLDV system can be processed by a modal analysis method to estimate modal parameters of a structure [21–27]. The lifting method estimates modal parameters, including damped natural frequencies, damping ratios, and undamped mode shapes, of a structure subject to random excitation [21,22]. The demodulation method estimates operational deflection shapes of a structure subject to sinusoidal excitation [23–25,28] or modal parameters, including damped natural frequencies and undamped mode shapes, of a structure subject to random excitation [29]. The above methods were developed for processing measurements obtained on straight-line scan paths to estimate one-dimensional (1D) modal parameters. In addition to laser Doppler vibrometry, a blade tip timing (BTT) technique is also a suitable noncontact method for vibration monitoring of a rotating structure [30,31]. The BTT technique can measuring vibrations of all blades at the same stage of an aero-engine in a non-intrusive manner. The technique is suitable for measuring vibrations of rotating structures with high speeds, such as aero-engines; however, it is difficult to use it for full-field vibration measurement of a rotating structure with high spatial resolution. To estimate full-field modal parameters of a structure, a two-dimensional (2D) scan scheme that can let a CSLDV system scan its whole surface was developed [32–34]. Point tracking methods were developed for laser Doppler vibrometer systems to track points on rotating structures by attaching encoders to rotating structures [35–38], and they were extended to tracking and continuously scanning methods to sweep laser spots of tracking CSLDV systems along prescribed scan paths on rotating structures [39–42]. Mirrors of tracking CSLDV systems need to be aligned with rotation axes of structures that are tracked and scanned when using the above tracking and continuously scanning methods [43–45]. A single-point tracking laser Doppler vibrometer system that tracks the position of a moving object by processing its images was developed to track a point on a windscreen wiper that was swung back and forth [46]. A tracking CSLDV system was developed to track a rotating fan blade by processing its images and scan along prescribed 1D or 2D paths on it [47–49]. These laser vibrometer systems track moving objects by attaching marks to them and processing their images to determine real-time positions of marks, which are difficult to use to track large rotating wind turbine blades since it is difficult to attach marks to wind turbine blades. An edge detection method was developed for an image-based tracking CSLDV system to track a rotating structure without attaching any encoder or mark to it [50], but this edge detection method works when images of the rotating structure have a simple background. A more robust image processing method is needed so that the image-based tracking CSLDV system can track and scan an actual rotating wind turbine blade with a complex background.

In this work, a novel robust edge detection method is developed for the image-based tracking CSLDV system in Refs. [47–50] for tracking and scanning a rotating structure with a complex background. A rotating fan blade, which is a model of a wind turbine blade under operational conditions, is tracked and scanned by the image-based tracking CSLDV system. A new 2D scan scheme is developed to sweep the laser spot along the whole surface of the rotating fan blade. The improved demodulation method in Refs. [48–50] is used to obtain damped natural frequencies and full-field undamped mode shapes of the rotating fan blade with different constant speeds.

The following sections of this paper are listed below. The robust edge detection method for the tracking CSLDV system is introduced in Sec. 2.1. A 2D scan scheme for the tracking CSLDV system is introduced in Sec. 2.2. The experimental setup is presented in Sec. 3.1. Edge detection and modal analysis results are presented in Secs. 3.2 and 3.3, respectively. Some conclusions are presented in Sec. 4.

2. Methodologies

2.1. Robust edge detection method

A background subtraction technique is implemented as an extension of the edge detection method used in Ref. [50]. Previously, a

black tarp shrouded the aluminum frame and background to facilitate image processing by providing a homogeneous colored area around the fan [47–50]. In this work, the black tarp is removed to instill a complex background. A complex background is used to better replicate real-world settings. Fig. 1 shows a comparison between frames with and without the black tarp background. Figs. 1(b) and 1(c) show that structural members of the aluminum frame are present around the rotation center of the fan.

In the current frame, edge detection alone shows edges of the fan and edges of the aluminum frame. Without removing the edges of the aluminum frame, edge detection does not provide an effective means of tracking the fan blades as they rotate. To remove all edges that do not constitute the edges of the fan blades, two consecutive video frames are used to form a differential frame by subtracting the previous frame from the current frame. The differential frame produced from this subtraction technique consists only of the angular motion made by the rotating fan blades. Pixels in a frame that constitute stationary objects retain their intensity values throughout a video sequence. Since digital images are matrices, simple matrix subtraction removes all stationary objects in the frame. When the camera is stationary and the largest moving object in the frame is the rotating fan, this background subtraction technique is effective for isolating the edges of the rotating fan blades.

Fig. 2 shows an illustration of the working principle behind the background subtraction technique. Consider two consecutive frames of a video sequence. Previous and current frames are denoted as P_{i-1} and P_i, respectively. The frame rate of the camera is sufficiently higher than the rotation speed of the fan. This allows small angular motions to be determined between two consecutive frames that are indicated by shaded regions in Fig. 2. The extracted sub-frame is shown in Fig. 2(b) to depict portions of the blade that

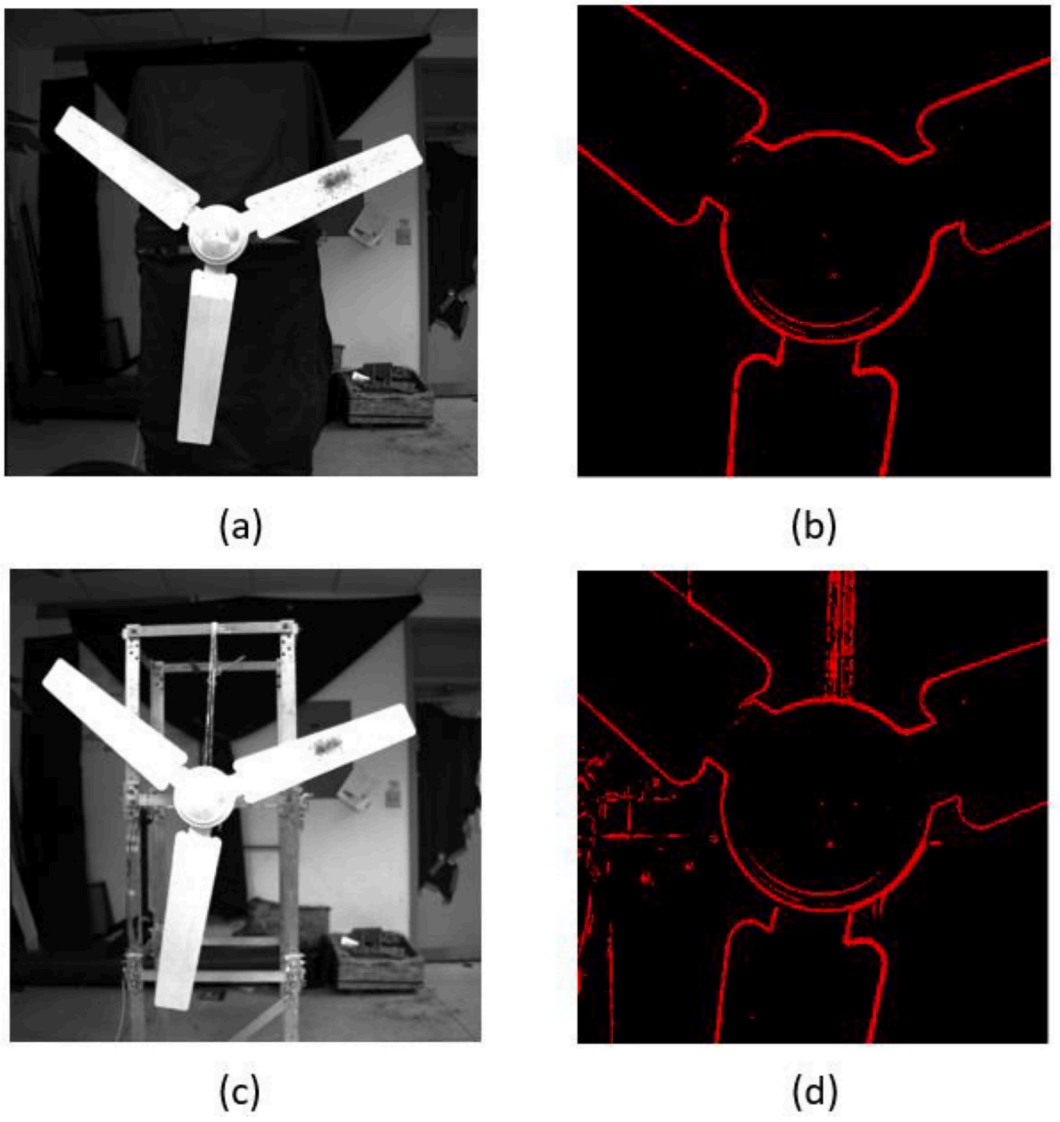

Fig. 1. (a) Image of the fan with a black background, (b) the edge map of the fan with the black background, (c) the image of the fan with a complex background, and (d) the edge map of the fan with the complex background.

are retained and removed in the differential frame.

In this work, the fan rotates in the counterclockwise direction in view of the camera, as indicated by the arrow in Fig. 2(a). The region of the blade labeled as (1) in Fig. 2(b) denotes the blade's positive angular motion. This is the region of the blade that is shown in the differential frame. Region (2) in Fig. 2(b) is the portion of overlapping blade positions between the current and previous frames, and the region denoted by (3) is the position of the blade in the previous frame. As previously stated, pixels that retain their intensity values between frames are removed when matrix subtraction is applied. This causes region (2) to be removed in the differential frame.

Region (3) is removed due to the difference in color between the blade and background. Consider the following example; the pixel values in an 8-bit image range from 0 to 255 where 0 represents no intensity (black) and 255 represents full intensity (white). Region (3) in Fig. 2(b) is the position of the blade in the previous frame, which has high pixel intensities. In the current frame, the blade is no longer in this position, and the pixel intensities are now those that constitute the background, i.e., lower intensity values. When matrix subtraction is applied, region (3) in the differential frame theoretically consists of negative intensity values. Since pixels cannot have negative values, region (3) is occupied by intensity values of zero instead of negative values. Because of this, region (3) is removed in the differential frame. Fig. 3 shows that edges of the aluminum frame are removed while the angular motion of the blades is retained.

Selecting dimensions of the sub-frame and values of radial bounds that are used for the distance condition discussed in Ref. [50] is up to the user, but some guidelines should be followed to ensure optimal performance. Using the sub-frame in this algorithm is motivated by a reduction in computational time, but there is a minimum size that can be selected so that the algorithm still performs as expected. The sub-frame is constructed using coordinates of the rotation center with two transformation constants (dx and dy) whose values are specified by the user. The illustration in Fig. 4(a) shows sub-frame dimensions constructed using rotation center coordinates in the XY coordinate system and transformation constants.

In this work, the transformation constants are chosen to be equal so that the sub-frame is a square. The sub-frame is now defined by new axes X' and Y', and radial bounds are defined relative to rotation center coordinates, which correspond to the center of the sub-frame, i.e., $(\frac{x'}{2}, \frac{y'}{2})$. The radial bounds in Fig. 4(b) are defined by radius values and should be chosen so that the radius of the outer radial bound r_o should be less than half the value of the sub-frame dimension (i.e., $r_o < \frac{y'}{2}$). The radius of the inner radial bound should be chosen to be less than the outer radial bound, but greater than any portion of the blades that has a non-uniform profile, which is typically a change in geometry near the point of attachment between the fan blades and center hub. Fig. 5(a) labels a point of non-uniform blade geometry that is considered in this work when selecting values for the radial bounds in Fig. 5(b).

When the algorithm runs in real time, the averaged location of edges around a detected edge is used as the current position of a fan blade. The actual position of the fan blade differs slightly from its calculated position due to some latency, but when the position is used to control the tracking CSLDV system, a phase angle is incorporated that allows the laser spot position to be adjusted so that the laser spot remains on the fan blade as it rotates.

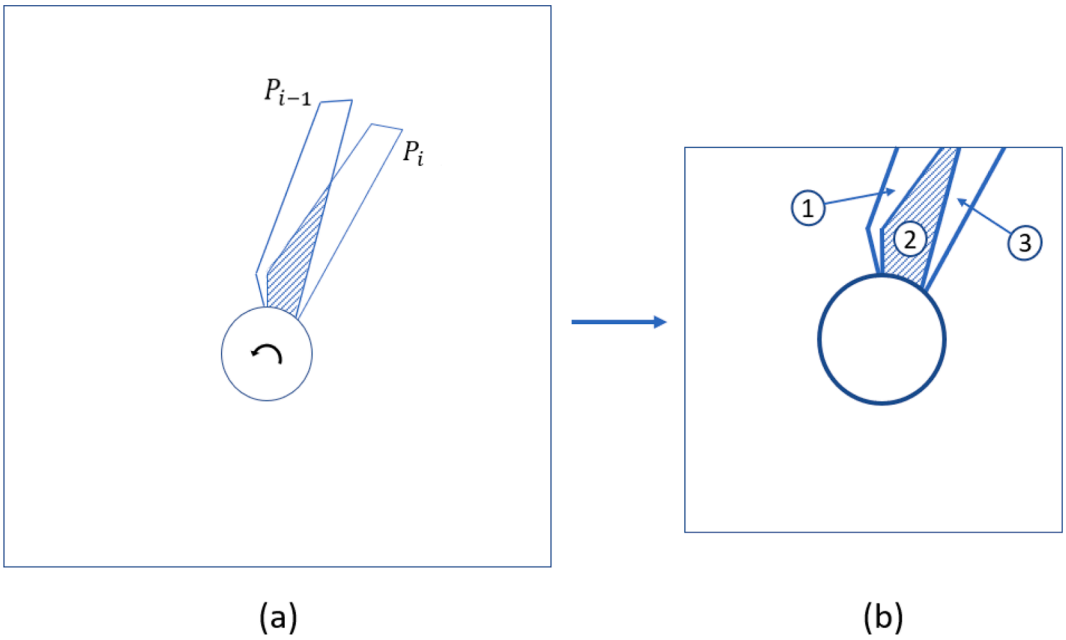

Fig. 2. (a) Illustration of the relative position of a single blade between two consecutive frames, and (b) three regions of consideration within the sub-frame made by the blade's positions between frames.

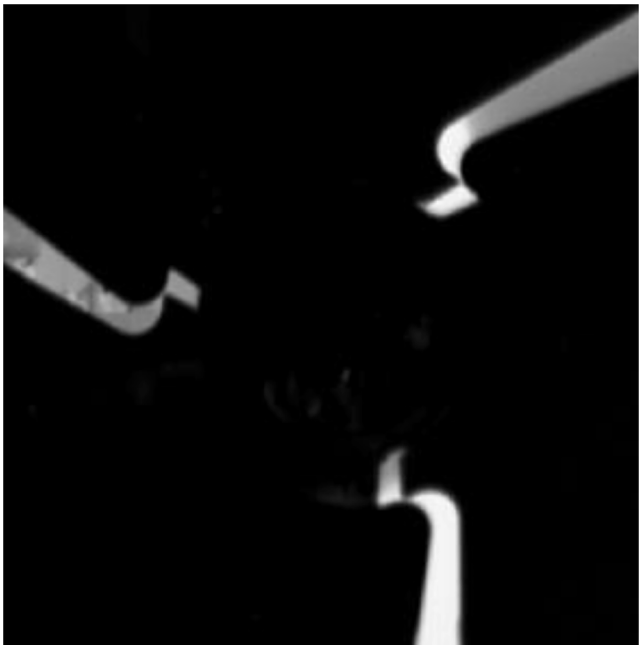

Fig. 3. A differential frame made by two consecutive frames by subtracting the previous frame from the current frame.

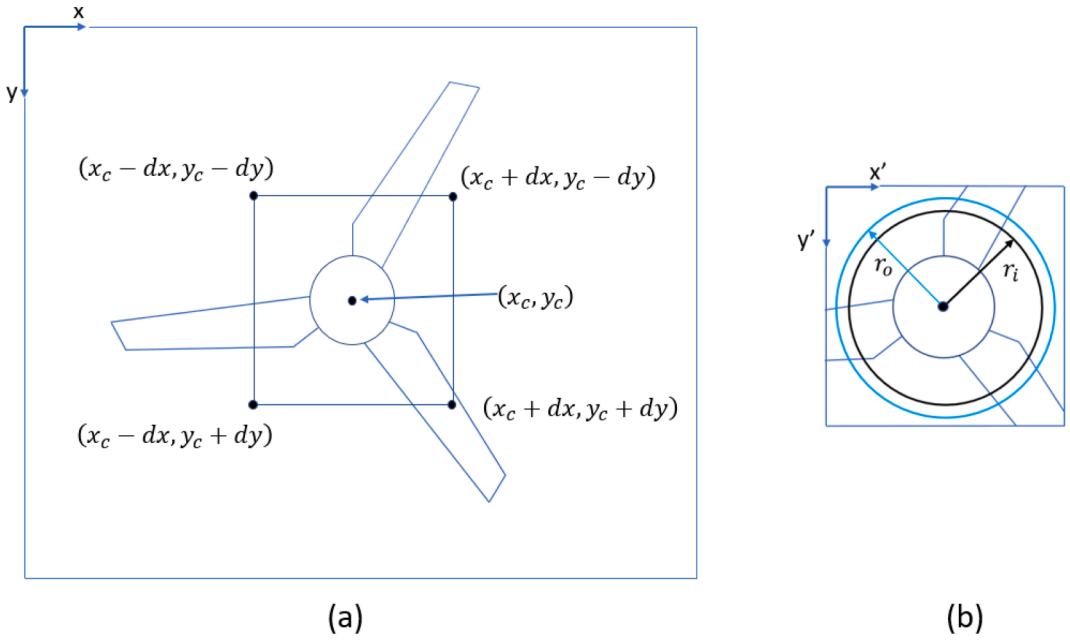

Fig. 4. (a) Illustration of using transformation constants to construct sub-frame dimensions around the rotation center, and (b) illustration of radial bounds defined within the extracted sub-frame.

2.2. 2D scan scheme

Once the position of an edge is determined by the method in Sec. 2.1, a 2D zigzag scan path can be generated on the rotating fan blade. Let coordinates of the detected edge of the rotating fan blade be (x_e, y_e), and coordinates of corners of the fan blade be (x_1, y_1), (x_2, y_2), (x_3, y_3), and (x_4, y_4), the 2D scan path is generated based on these coordinates (Fig. 6(a)). Note that the schematic of the rotating fan blade in Fig. 6 has a general quadrilateral shape to demonstrate the scan scheme on an arbitrary quadrilateral rotating blade. Once (x_e, y_e) is determined by the robust edge detection method, one can shift (x_e, y_e) to (x'_e, y'_e), which is within the boundary of

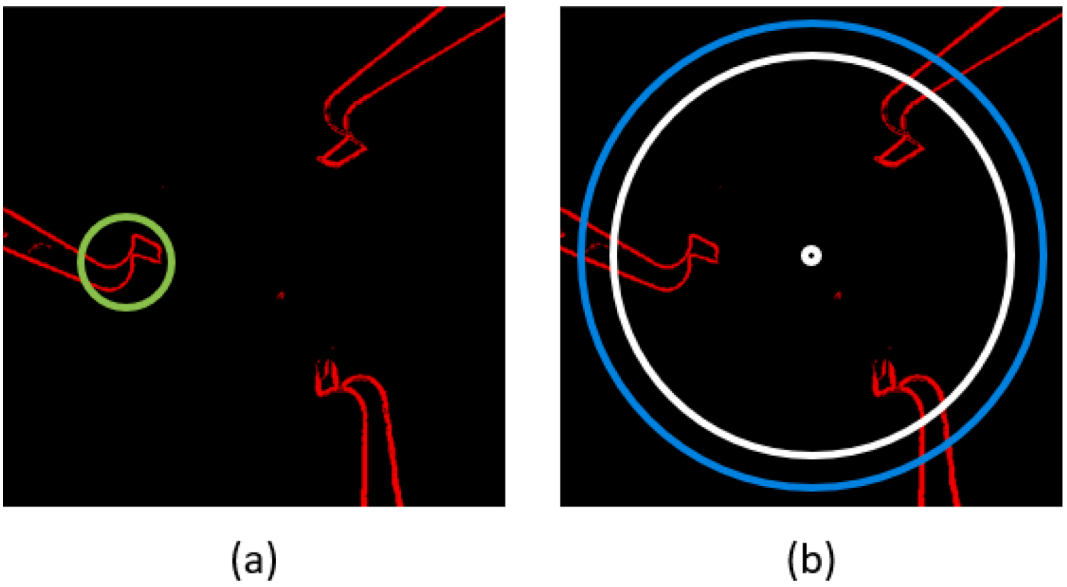

Fig. 5. (a) Edge map from applying edge detection to the differential frame in Fig. 3 with the fan blade's non-uniform geometry indicated by the circle, and (b) radial bounds defined to exclude the non-uniform geometry portion of the fan blades.

the blade (Fig. 6(b)), by

$$\begin{cases} x'_e = x_c + C[(x_e - x_c)\cos(\theta) + (y_e - y_c)\sin(\theta)\,] \\ y'_e = y_c + C[\,-(x_e - x_c)\sin(\theta) + (y_e - y_c)\cos(\theta)\,] \end{cases} \tag{1}$$

where C is a constant that is used to adjust the distance between (x_c, y_c) and (x'_e, y'_e), and θ is the angle between the line that passes through (x_c, y_c) and (x_e, y_e), and the line that passes through (x_c, y_c) and (x'_e, y'_e). The distance between (x'_e, y'_e) and (x_c, y_c) is calculated by $r = \sqrt{(x'_e - x_c)^2 + (y'_e - y_c)^2}$. Once C and θ are fixed, one can calculate coordinates of four corners of the rotating blade based on its geometry. Coordinates of projections of four corners of the rotating blade on the line that passes though (x_c, y_c) and (x'_e, y'_e) can be determined since (x_c, y_c) and (x'_e, y'_e) are known. Let distances between projections of four corners of the rotating blade and (x_c, y_c) be s_1, s_2, s_3, and s_4, respectively, and distances between four corners of the rotating blade and the line that passes though (x_c, y_c) and (x'_e, y'_e) be a, b, c, and d, respectively; one can calculate coordinates of the four corners by

$$\begin{cases} x_1 = x_c + s_1(x'_e - x_c)/r + a(y'_e - y_c)/r \\ y_1 = y_c + s_1(y'_e - y_c)/r - a(x'_e - x_c)/r \end{cases} \tag{2}$$

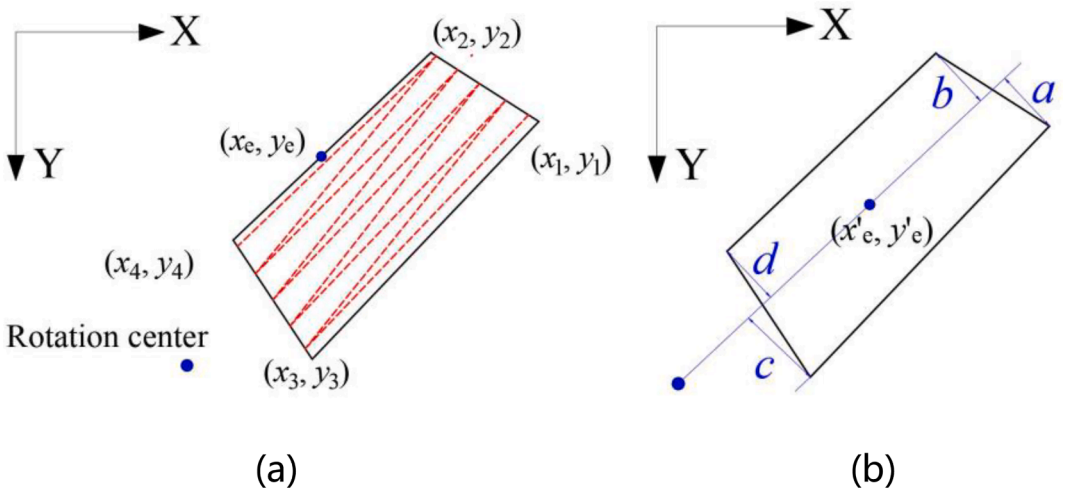

Fig. 6. (a) Scan path generated on the rotating blade, and (b) the shifted edge point on the rotating blade.

$$\begin{cases} x_2 = x_c + s_2(x'_e - x_c)/r - b(y'_e - y_c)/r \\ y_2 = y_c + s_2(x'_e - x_c)/r + b(x'_e - x_c)/r \end{cases} \tag{3}$$

$$\begin{cases} x_3 = x_c + s_3(x'_e - x_c)/r + c(y'_e - y_c)/r \\ y_3 = y_c + s_3(x'_e - x_c)/r - c(x'_e - x_c)/r \end{cases} \tag{4}$$

$$\begin{cases} x_4 = x_c + s_4(x'_e - x_c)/r - d(y'_e - y_c)/r \\ y_4 = y_c + s_4(x'_e - x_c)/r + d(x'_e - x_c)/r \end{cases} \tag{5}$$

The zigzag scan path is a combination of multiple straight lines. The laser spot of the image-based tracking CSLDV system is swept on each line for an odd number of times when tracking and scanning the rotating blade. Coordinates of four corners of the rotating blade can be used to generate end points of the current line swept by the laser spot. The 2D scan scheme uses four distances to control positions of four boundary points of a 2D scan path, which is more intuitive than the 2D scan scheme in Ref. [47] that uses four angles to control positions of four boundary points of a 2D scan path.

Let the laser spot be swept on N lines; coordinates of end points of the i -th line (x_i^1, y_i^1) and (x_i^2, y_i^2) can be determined by [49]

$$\begin{cases} x_i^1 = y_2 + \dfrac{2(x_1 - x_2)}{N-1}\left(\dfrac{N-i}{2}\right) \\ y_i^1 = y_2 + \dfrac{2(y_1 - y_2)}{N-1}\left(\dfrac{N-i}{2}\right) \end{cases} \tag{6}$$

$$\begin{cases} x_i^2 = x_4 + \dfrac{2(x_3 - x_4)}{N-1}\left(\dfrac{N-i}{2}\right) \\ y_i^2 = y_4 + \dfrac{2(y_3 - y_4)}{N-1}\left(\dfrac{N-i}{2}\right) \end{cases} \tag{7}$$

when i is odd, and

$$\begin{cases} x_i^1 = y_2 + \dfrac{2(x_1 - x_2)}{N-1}\left(\dfrac{N-i-1}{2}\right) \\ y_i^1 = y_2 + \dfrac{2(y_1 - y_2)}{N-1}\left(\dfrac{N-i-1}{2}\right) \end{cases} \tag{8}$$

$$\begin{cases} x_i^2 = x_4 + \dfrac{2(x_3 - x_4)}{N-1}\left(\dfrac{N-i+1}{2}\right) \\ y_i^2 = y_4 + \dfrac{2(y_3 - y_4)}{N-1}\left(\dfrac{N-i+1}{2}\right) \end{cases} \tag{9}$$

when i is even. The laser spot is swept between (x_i^1, y_i^1) and (x_i^2, y_i^2) when the image-based tracking CSLDV system tracks the rotating blade. The image-based tracking CSLDV system measures responses of the rotating blade when tracking and scanning it, and an improved demodulation method based on a non-uniform rotating plate vibration theory in Ref. [47] can process measured responses to

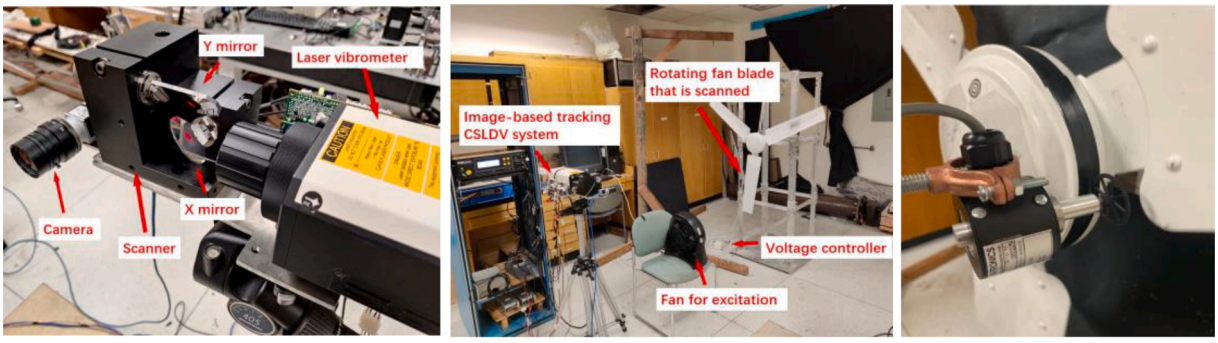

Fig. 7. (a) Components in the image-based tracking CSLDV system, (b) the experimental setup of tracking and scanning a rotating fan blade with a complex background, and (c) a rotary encoder that was attached to the fan hub for rotation speed measurement for validation purposes.

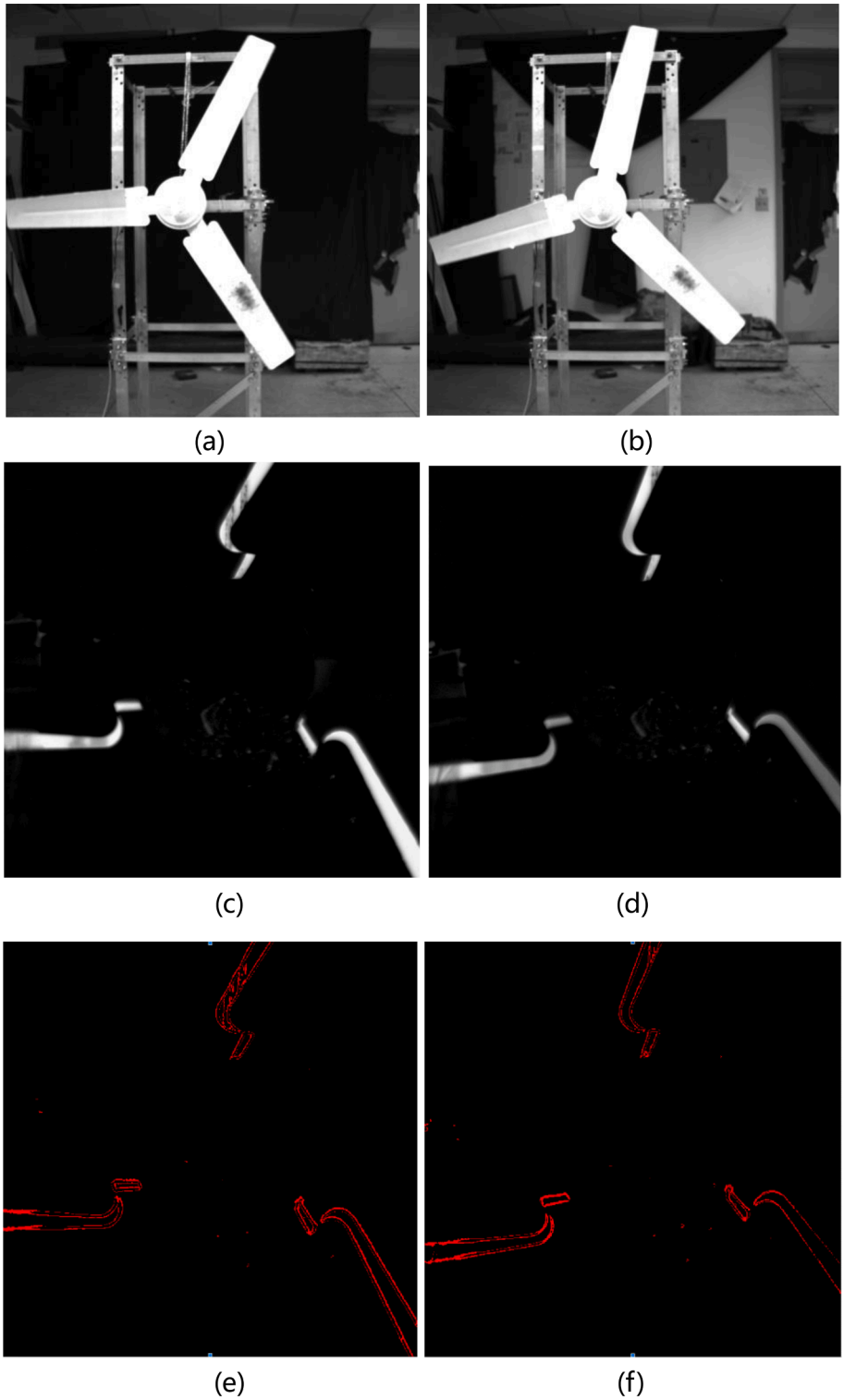

Fig. 8. Images of the rotating fan captured by the camera in the image-based tracking CSLDV system with the black tarp (a) covered and (b) removed, differential frames obtained from images captured by the camera with the black tarp (c) covered and (d) removed, (e) the edge map from applying Sobel edge detection to (c), and (f) the edge map from applying Sobel edge detection to (d).

obtain full-field undamped mode shapes of the rotating blade.

Measured (x_e, y_e) are also used to estimate the real-time rotation speed of the blade. Let $(x_e(t_1), y_e(t_1))$ and $(x_e(t_2), y_e(t_2))$ be estimated edge positions at time instants t_1 and t_2, respectively; one can calculate the rotation speed of the rotating blade by

$$R = \frac{1}{t_2 - t_1} \arccos\left(\frac{(x_e(t_1) - x_c)(x_e(t_2) - x_c) + (y_e(t_1) - y_c)(y_e(t_2) - y_c)}{\sqrt{[(x_e(t_1) - x_c)^2 + (y_e(t_1) - y_c)^2)][(x_e(t_2) - x_c)^2 + (y_e(t_2) - y_c)^2)]} } \right) \tag{10}$$

3. Experimental investigation

3.1. Experimental setup

The image-based tracking CSLDV is shown in Fig. 7(a), which consists of a Polytec OFV-353 single-point laser vibrometer, a Cambridge 6240H scanner with a set of orthogonal mirrors, and a Basler acA2040-90um camera. The experimental setup of tracking and full-field scanning of a rotating fan blade under random excitation is shown in Fig. 7(b). The fan was mounted on a frame with a hub height of 123.5 cm. The blade that was tracked and scanned by the image-based tracking CSLDV system was covered by a reflective tape so that the signal-to-noise ratio of measurement of the image-based tracking CSLDV system was sufficiently high. The frame and the wall behind it could provide a complex background to all images captured by the camera (Fig. 7(b)). The image-based tracking CSLDV system was mounted on a tripod with a height of 116.6 cm. The distance between mirrors of the image-based tracking CSLDV

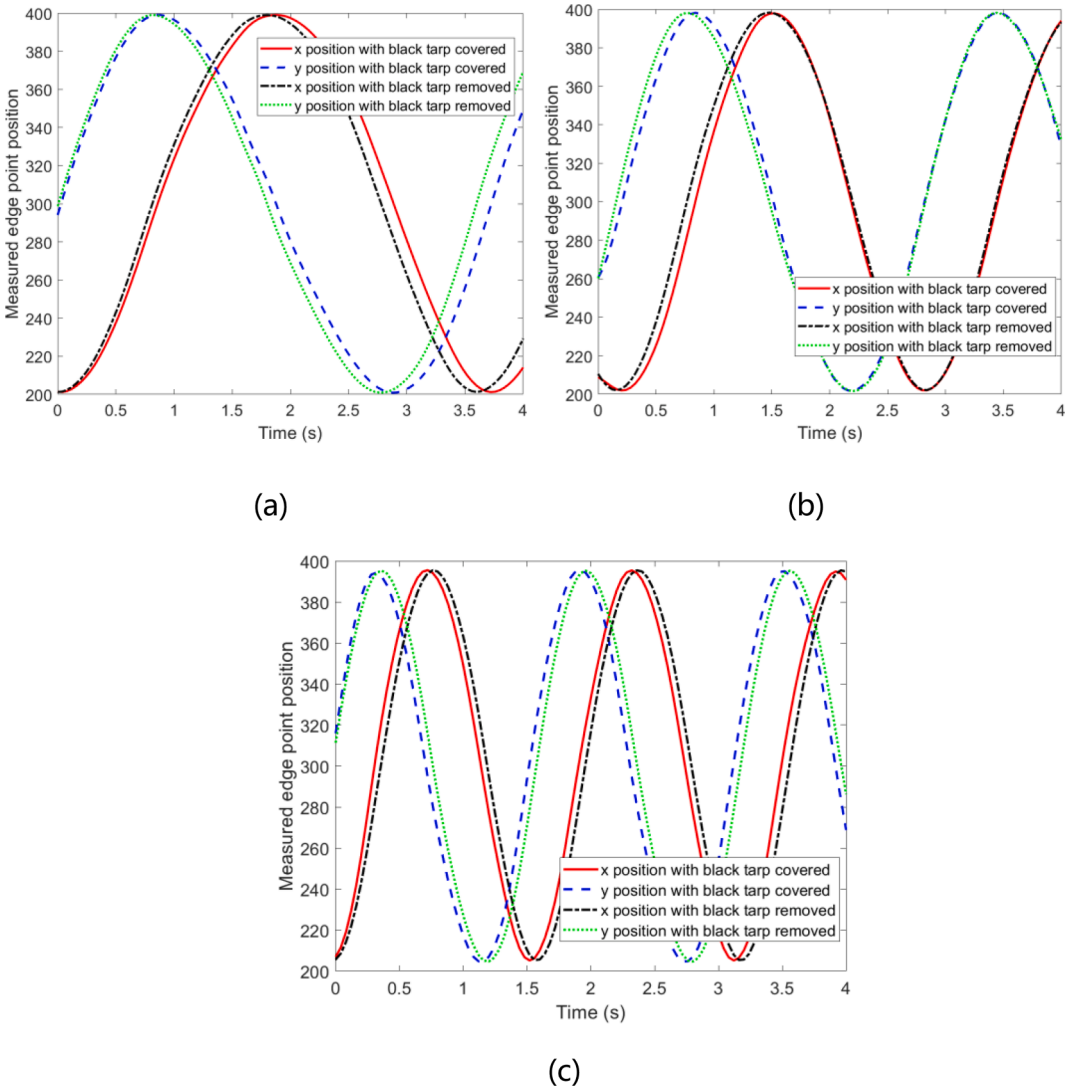

Fig. 9. Estimated edge positions of a rotating fan blade with (a) low, (b) medium, and (c) high speeds.

system and the fan was 173.8 cm. A small fan that was 92 cm away from the fan was used to excite the fan blades by its air flow. The air flow of the small fan could be considered as random excitation applied to the fan blades. The camera captured images of the fan with a pixel resolution of 2048 × 2048 and a frame rate of 50 frames per second. A camera with a higher pixel resolution can increase the accuracy of estimated locations of edges of the rotating fan blade, which can generate a scan path with a higher position accuracy, but can lead to an increased image processing time. When the fan was stationary, the position of a fan blade could be easily determined in an image of the fan. A prescribed stationary 2D scan scheme could be generated on the fan blade so that the image-based tracking CSLDV system could scan its whole surface. When the fan was turned on and rotated with a constant speed, the camera kept capturing its images. When an image of the rotating fan was captured, the robust edge detection method introduced in Sec. 2.1 could remove the complex background in it and determine the position of an edge of a rotating fan blade. The position was shifted to a position on the middle line of the rotating fan blade. The 2D scan scheme in Sec. 2.2 calculated positions of four corners of the fan blade that was scanned and determined endpoints of the line that the laser spot was swept on. Angular positions of orthogonal mirrors of the scanner were considered to be linearly related to X and Y positions of the laser spot when rotation angles of orthogonal mirrors were small. Orthogonal mirrors of the scanner were controlled to rotate by an NI9149 controller to change the position of the laser spot based on positions of end points of the line. A fan speed controller was used to let the fan rotate with different constant speeds. A rotary encoder that was attached to the fan hub was used to validate the edge detection method by comparing estimated rotation speeds of the fan blade from the edge detection method and rotary encoder (Fig. 7(c)). The image-based tracking CSLDV system could track and scan the rotating fan blade whose speed was between 0 and 40 revolutions per minute (rpm); therefore, it can easily track and scan a rotating wind turbine blade with a speed of 5–15 rpm [49]. Note that it is difficult to use the image-based tracking CSLDV system to track and scan a rotating structure with a high speed, such as a rotating aero-engine blade.

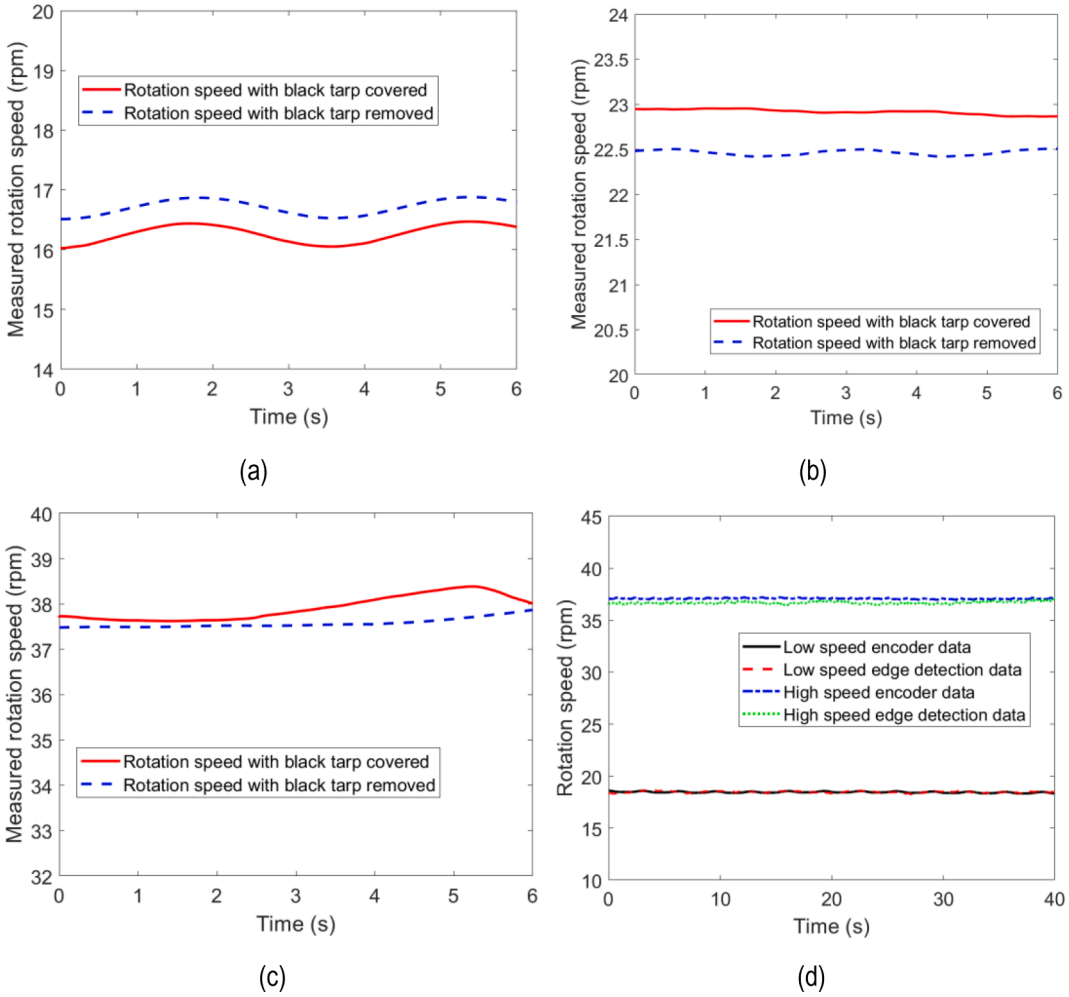

Fig. 10. Estimated rotation speeds of the rotating fan blade with (a) low, (b) medium, and (c) high speeds, and (d) estimated rotation speeds of the rotating fan blade using the edge detection method and rotary encoder.

3.2. Edge detection results

To validate the robustness of the edge detection method, the fan was turned on and rotated with a constant speed. The edge detection method was used to track a rotating fan blade and estimate its rotation speed with the black tarp on the wall behind the frame covered and removed. Estimated speeds of the rotating fan blade with the black tarp covered and removed were compared. Images of the rotating fan with a constant speed captured by the camera in the image-based tracking CSLDV system are shown in Figs. 8(a) and 8 (b). Differential frames obtained from images captured by the camera are shown in Figs. 8(c) and 8(d), where edges of the rotating fan are clearly shown while backgrounds are basically removed. Sobel detector was applied to Figs. 8(c) and 8(d) and their resultant edge maps are shown in Figs. 8(e) and 8(f), respectively. Edge positions could be easily determined in both edge maps in Fig. 8 by the robust edge detection method. Note that edges of all three blades of the rotating fan are shown in edge maps. To track the position of one blade of the rotating fan, one needs to use the distance condition described in Ref. [50].

Estimated edge positions in the X'Y′ coordinate system of a rotating fan blade with low, medium, and high constant speeds are shown in Fig. 9. Plots were shifted to minimize phase differences between edge positions with the black tarp covered and edge positions with the black tarp removed. Estimated edge positions of the rotating fan blade with the black tarp covered and removed are close to each other, which means that backgrounds of images captured by the camera did not affect tracking of the rotating fan blade.

Estimated speeds of the rotating fan blade from Fig. 9 are shown in Figs. 10(a), 10(b), and 10(c), where rotation speeds with the black tarp covered are close to those with the black tarp removed. Calculated averaged rotation speeds and errors between rotation speeds with the black tarp covered and removed are listed in Table 1, where each averaged rotation speed is calculated from 151 data in 6 s. One can see that the error between estimated low rotation speeds with the black tarp covered and removed is larger than the error between estimated high rotation speeds. Blades of the rotating fan were not in balance since the blade that was covered with a reflective tape, and the fan could not fully maintain a constant low speed due to insufficient power that was controlled by the fan speed controller, which caused a larger error between estimated lower rotation speeds with the black tarp covered and removed. Estimated speeds of the rotating fan blade from the edge detection method and rotary encoder are shown in Fig. 10(d) and Table 2, where each averaged rotation speed is calculated from 3239 data in 40 s. Estimated speeds of the rotating fan blade are close to each other with differences of 0.65% and 1.05% for two rotation speeds. The edge detection method can accurately estimate locations of edges of the rotating fan blade, which can generate accurate scan paths, and the resolution of images is high enough for experiments conducted.

A comparison of edge detection results with different misalignments is shown in Figs. 11 and 12, where the small misalignment means that the optical axis of the camera and the rotation axis of the fan blade are basically parallel to each other, with the angle between the optical axis of the camera and the rotation axis of the fan blade being about 4.6°, the 15° misalignment means that the angle between the optical axis of the camera and the rotation axis of the fan blade is about 15°, and the 30° misalignment means that the angle between the optical axis of the camera and the rotation axis of the fan blade is about 30°.

The fan was turned on and rotated with a constant speed for comparison of edge detection and operational modal analysis (OMA) results with different misalignments. Estimated edge positions of the rotating fan blade with different misalignments are shown in Fig. 12, where edge positions are basically close to each other. Estimated edge positions of the rotating fan blade with the 30° misalignment are slightly different from the other estimated edge positions due to the larger misalignment.

Estimated rotation speeds from edge positions in Fig. 12 are shown in Fig. 13(a), and averaged rotation speeds are shown in Table 3. The difference between averaged rotation speeds of the fan blade with the small misalignment and the 15° misalignment is 0.78%, and the difference between average rotation speeds of the fan blade with the small misalignment and the 30° misalignment is 3.9%. The difference between the second damped natural frequencies of the fan blade with the small misalignment and the 15° misalignment is 0.2%, and the difference between the second damped natural frequencies of the fan blade with the small misalignment and the 30° misalignment is 0.55%. The estimated 1D second undamped mode shapes of the rotating fan blade on a straight-line scan path in the middle of the blade along its length direction with different misalignments are shown in Fig. 13(b). The modal assurance criterion (MAC) value between the second undamped mode shapes of the fan blade with the small misalignment and the 15° misalignment is 98.05%, and the MAC value between the second undamped mode shape of the fan blade with the small misalignment and the 30° misalignment is 96.39%, which are acceptable for OMA. Note that the average hub height and rotor diameter of current land-based wind turbines are about 94 m and 127.5 m, respectively [51], and a long-range laser vibrometer can measure the vibration of a structure up to 300 m away [52]. If one places the long-range laser vibrometer 200 m away from a wind turbine with the average hub height and rotor diameter, the angle between the optical axis of the camera and the rotation axis of the wind turbine is about 25.17°, and the maximum distance between the long-range laser vibrometer and the tip of a rotating wind turbine blade is about 254.72 m, which are acceptable for the long-range laser vibrometer and the current edge detection method based on the above comparison results. A field test of a real wind turbine blade will be conducted in the future and one may improve the edge detection method by compensating the effect of perspective projections that can cause large misalignment.

Table 1
Estimated averaged speeds and standard deviations σ of the rotating fan blade with different constant speeds and black tarp covered and removed.

Speed	Low	Medium	High
Black tarp covered	16.24 rpm (σ = 0.147)	22.90 rpm (σ = 0.028)	37.90 rpm (σ = 0.370)
Black tarp removed	16.69 rpm (σ = 0.126)	22.46 rpm (σ = 0.028)	37.57 rpm (σ = 0.099)
Difference	2.8%	1.9%	0.87%

Table 2
Estimated averaged speeds and standard deviations σ of the rotating fan blade using the edge detection method and the rotary encoder.

Fan speed	Edge detection	Encoder	Difference
Low	18.56 rpm ($\sigma = 0.082$)	18.44 rpm ($\sigma = 0.060$)	0.65%
High	36.67 rpm ($\sigma = 0.115$)	37.06 rpm ($\sigma = 0.049$)	1.05%

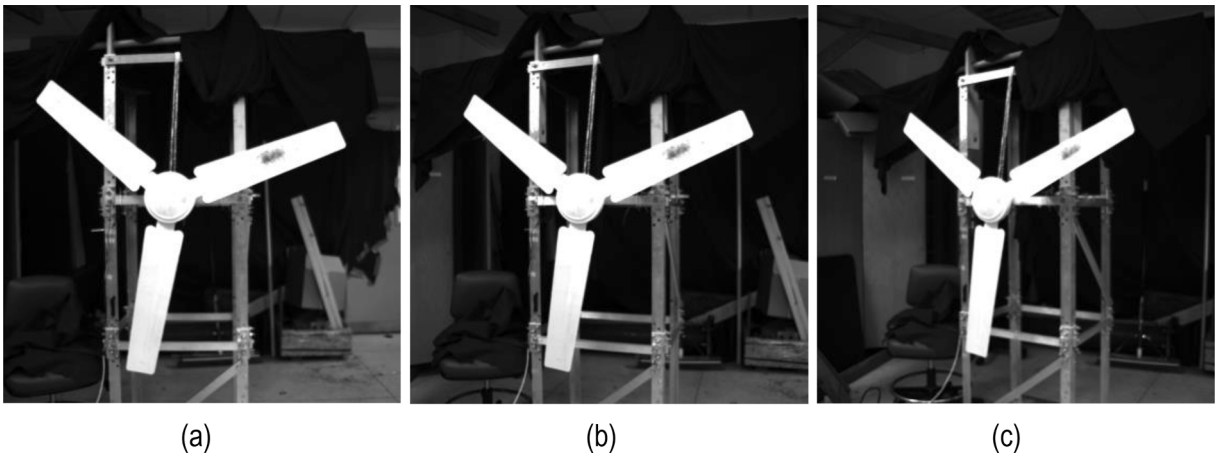

Fig. 11. Images of the rotating fan captured by the camera in the image-based tracking CSLDV system with (a) a small misalignment, (b) a 15° misalignment, and (c) a 30° misalignment.

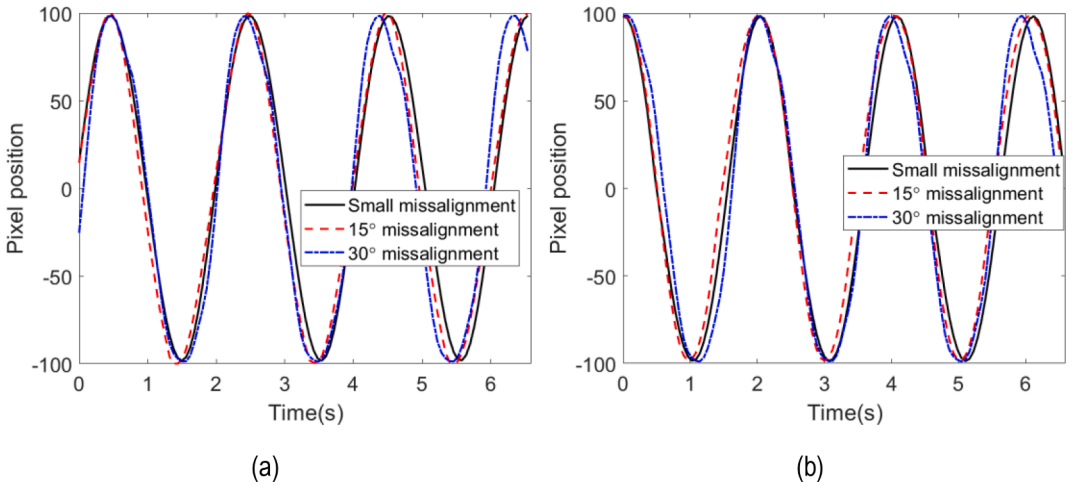

Fig. 12. Estimated (a) x and (b) y positions of the rotating fan blade with the small misalignment, the 15° misalignment, and the 30° misalignment.

3.3. OMA results

The 2D scan path that was used to scan the whole surface of the fan blade consisted of 30 lines, and the laser spot was swept along each line five times when tracking and scanning the fan blade. Measured responses of the image-based tracking CSLDV system when the fan was stationary and had two constant speeds $R = 18.95$ rpm and $R = 24.30$ rpm were used to estimate modal parameters of the fan blade. Measured responses of the stationary fan blade and the rotating fan blade with $R = 18.95$ rpm and $R = 24.30$ are shown in Figs. 14(a), 14(b), and 14(c), respectively. Note that measured responses of the rotating fan in Figs. 14(b) and 14(c) were preprocessed by a high-pass filter to remove pseudo vibrations caused by a misalignment between the rotation axis of the fan and the laser beam reflected by mirrors of the scanner with zero rotation angles [48]. Estimated real-time speeds of the stationary fan blade and the rotating fan blade with $R = 18.95$ rpm and $R = 24.30$ are shown in Fig. 14(d). The fast Fourier transform was applied to the measured response of a fan blade to estimate its damped natural frequencies. The first two damped natural frequencies of the stationary fan blade and the rotating fan blade with $R = 18.95$ rpm and $R = 24.30$ rpm are shown in Table 4. One can see that damped natural frequencies

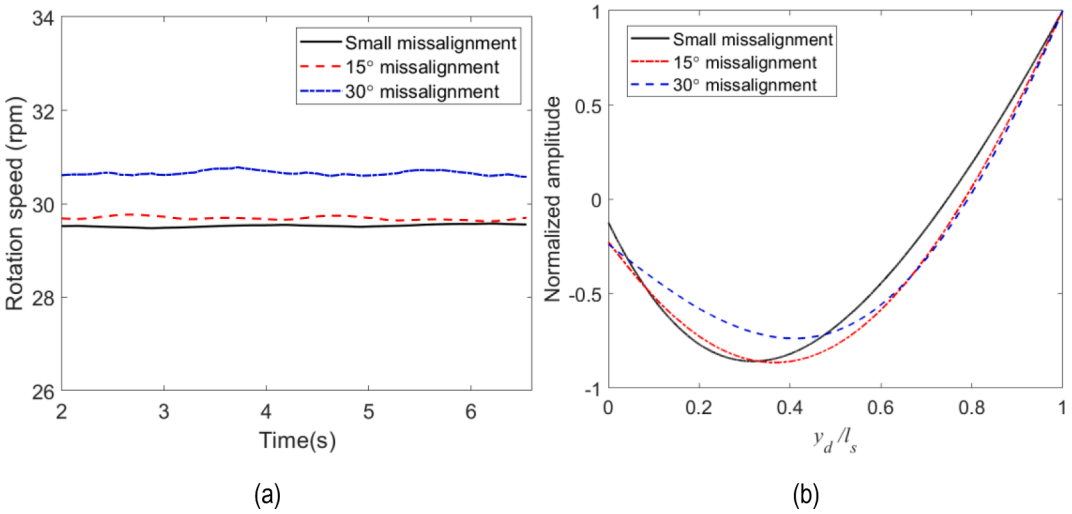

Fig. 13. (a) Estimated rotation speeds of the fan blade with different misalignments, and (b) estimated 1D second undamped mode shapes of the rotating fan blade along the straight-line scan path in the middle of the blade.

Table 3
Estimated averaged speeds, standard deviations σ, and damped natural frequencies of the rotating fan blade with different misalignments.

	Small misalignment	15° misalignment	30° misalignment
Averaged rotation speed (rpm)	29.50 ($\sigma = 0.023$)	29.73 ($\sigma = 0.046$)	30.65 ($\sigma = 0.048$)
Second damped natural frequency (Hz)	28.83	28.89	28.99

became higher when the fan blade rotated with a higher speed, which was caused by the centrifugal stiffening effect from rotation of the fan blade. The relation between damped natural frequencies and the rotation speed of a plate was derived in Ref. [49] where damped natural frequencies of the rotating plate increased with its speed, which was consistent with the results in this work. A similar relation between damped natural frequencies and the rotation speed caused by the centrifugal stiffening effect was found from experimental results in Ref. [41].

The improved demodulation method in Sec. 2.3 was used to process measurements of the image-based tracking CSLDV system. The first two undamped full-field mode shapes of the stationary fan blade are shown in Figs. 15(a) and 15(b), respectively, the first two undamped full-field mode shapes of the rotating fan blade with $R = 18.95$ rpm are shown in Figs. 15(c) and 15(d), respectively, and the first two undamped full-field mode shapes of the rotating fan blade with $R = 24.30$ rpm are shown in Figs. 15(e) and 15(f), respectively.

Undamped full-field mode shapes of the rotating fan blade are similar to the first two undamped bending mode shapes of a cantilever plate since the rotating fan blade is similar to a rotating cantilever plate whose one side is fixed at the fan hub. Vibrations corresponding to higher modes of the rotating fan blade have low signal-to-noise ratios in measurements of the image-based tracking CSLDV system, which requires the system to sweep its laser spot along each line many times so that some random noise can be removed by signal averaging and signal-to-noise ratios can be increased. This can greatly increase amounts of measurement data of the image-based tracking CSLDV system, which can greatly increase times for testing and signal processing. Therefore, only the first two modes of the rotating fan blade were estimated. The image-based tracking CSLDV system can estimate bending and torsional modes of a rotating wind turbine blade. Note that an actual wind turbine blade can have edgewise mode shapes [53,54], which requires a three-dimensional CSLDV system to estimate them [55]. Overall, main advantages of the proposed approach are that it does not need to have the axis of the camera to be parallel to the rotation axis of the wind turbine blade, and one does not need to have an encoder attached to the hub of the wind turbine. A disadvantage of the approach is that the rotation speed of the blade can be restricted to being lower than 40 rpm.

4. Conclusions

A robust edge detection method is developed for the image-based tracking CSLDV system to track and scan a rotating structure with a complex background. The robust edge detection method can remove the complex background in images captured by the camera in the image-based tracking CSLDV system and determine the position of an edge of the rotating structure. A 2D scan scheme is developed that can generate a zigzag scan path on the surface of the rotating structure based on the position of the edge. The laser spot of the image-based tracking CSLDV system is swept along the 2D scan path to measure the vibration of the rotating structure. An improved demodulation method is used to estimate modal parameters, including damped natural frequencies and undamped mode shapes, of the rotating structure. Experimental investigation of the robust edge detection method is conducted by tracking a rotating fan blade with a

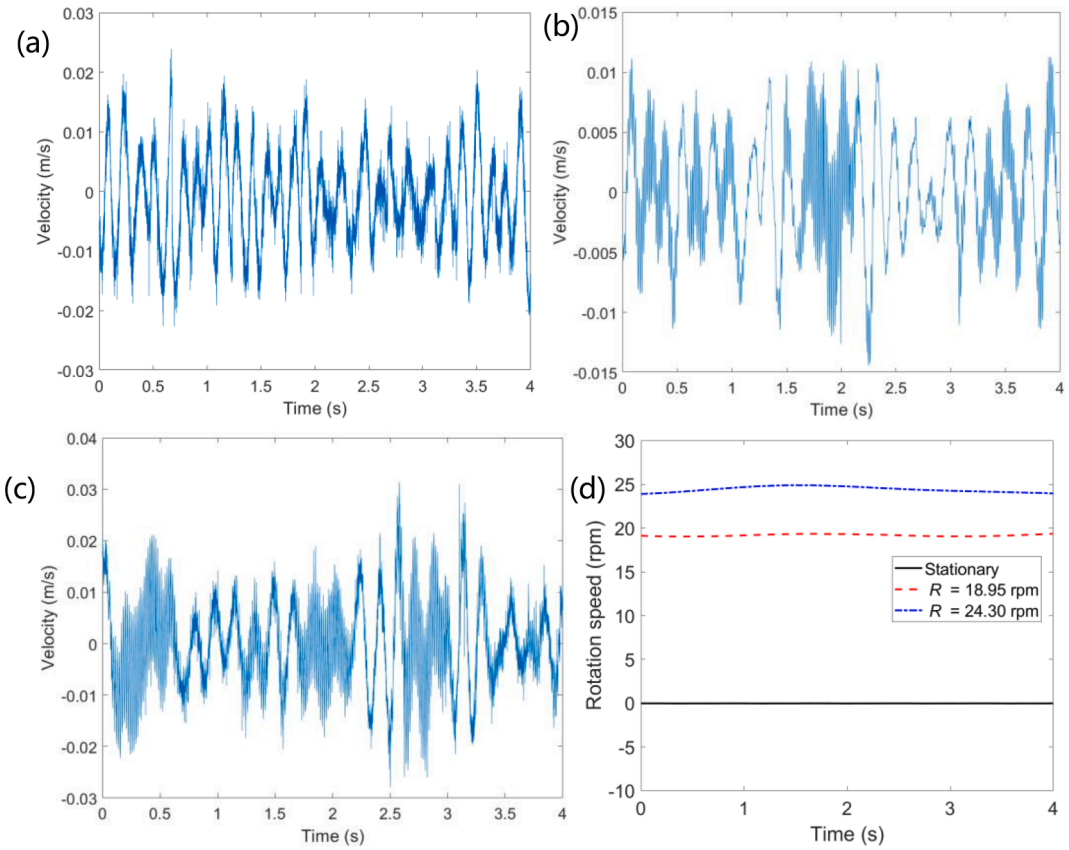

Fig. 14. Measured responses of the image-based tracking CSLDV system when (a) the fan was stationary and had two constant speeds (b) $R = 18.95$ rpm and (c) $R = 24.30$ rpm, and (d) estimated rotation speeds of the fan.

Table 4
Estimated damped natural frequencies of the rotating fan blade with different constant speeds.

Rotation speed	Stationary	18.95 rpm	24.30 rpm
First damped natural frequency (Hz)	6.40	6.75	6.90
Second damped natural frequency (Hz)	28.50	29.12	29.40

complex background and estimating the position of its edge as well as its rotation speed. Estimated rotation speeds of the fan blade from the edge detection method are validated by results from a rotary encoder. An angle between the optical axis of the camera and the rotation axis of the fan blade of up to 30°, which is relevant for real wind turbine testing, does not significantly affect edge detection and OMA results. The image-based tracking CSLDV system is used to estimate modal parameters of the stationary fan blade and the rotating fan blade with constant speeds. The first two damped natural frequencies and full-field undamped mode shapes of the stationary fan blade and the rotating fan blade with different constant speeds are successfully estimated. The image-based tracking CSLDV system will be used to track and scan real wind turbine blades and monitor their vibrations.

CRediT authorship contribution statement

L.F. Lyu: Methodology, Software, Validation, Writing – original draft. **G.D. Higgins:** Methodology, Software, Validation, Writing – original draft. **W.D. Zhu:** Conceptualization, Methodology, Funding acquisition, Supervision, Writing – review & editing.

Declaration of Competing Interest

The authors declare that they have no known competing financial interests or personal relationships that could have appeared to influence the work reported in this paper.

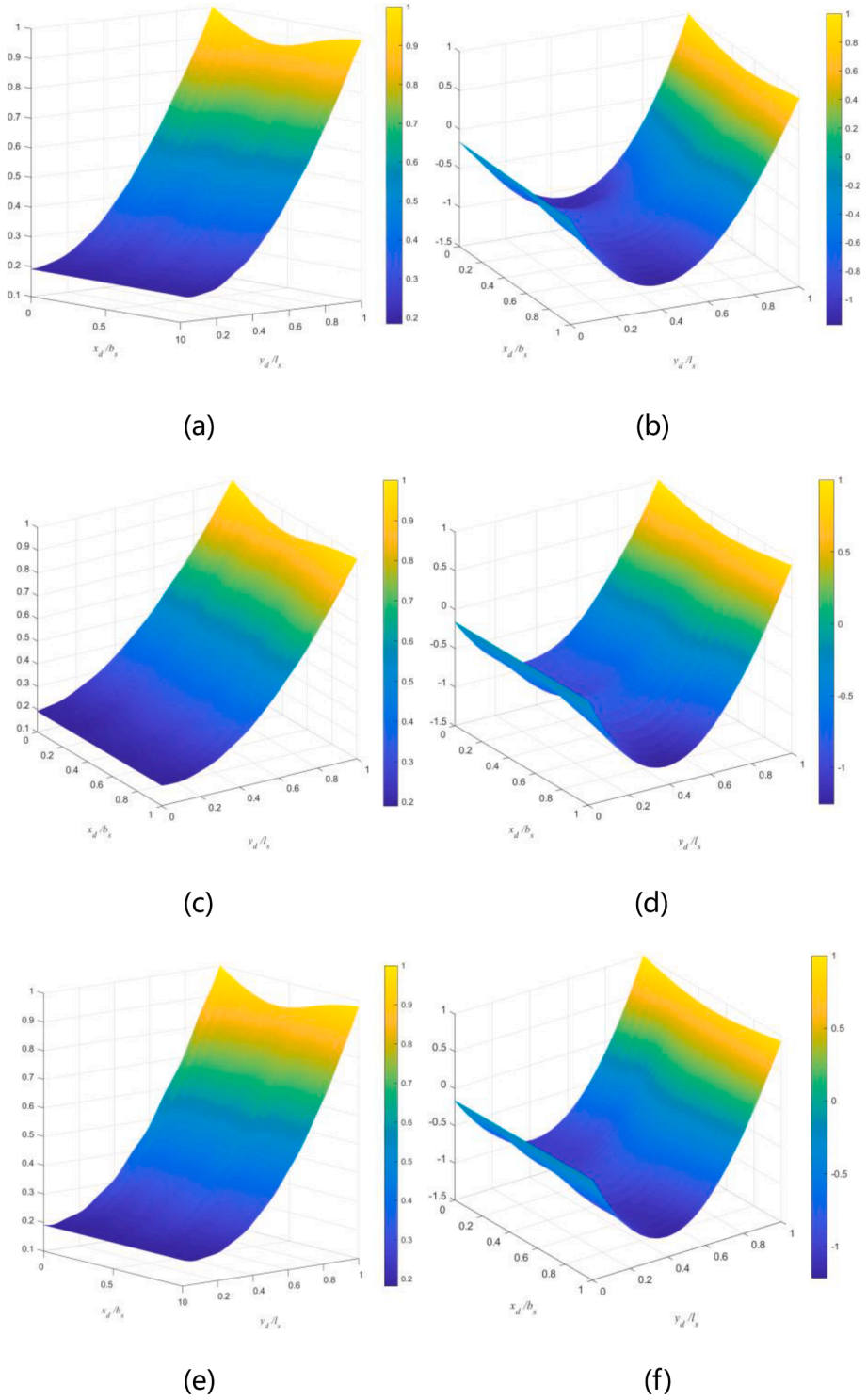

Fig. 15. Estimated (a) first and (b) second undamped mode shapes of the stationary fan blade, estimated (c) first and (d) second undamped mode shapes of the rotating fan blade with $R = 18.95$ rpm, and estimated (e) first and (f) second undamped mode shapes of the rotating fan blade with $R = 24.30$ rpm.

Data availability

Data will be made available on request.

Acknowledgment

This work is supported by the National Science Foundation through Grant No. CMMI-1763024.

References

[1] R.H. Wiser, M. Bolinger, B. Hoen, D. Millstein, J. Rand, G.L. Barbose, N.R. Darghouth, W. Gorman, S. Jeong, A.D. Mills, B. Paulos, Land-based wind market report: 2021 edition., Lawrence Berkeley National Lab, Berkeley, CA (United States) (2021), https://doi.org/10.2172/1818277.
[2] L. Mishnaevsky Jr, K. Thomsen, Costs of repair of wind turbine blades: Influence of technology aspects, Wind Energy 23 (12) (2020) 2247–2255, https://doi.org/10.1002/we.2552.
[3] J.I. Bech, C.B. Hasager, C. Bak, Extending the life of wind turbine blade leading edges by reducing the tip speed during extreme precipitation events, Wind Energy Science 3 (2) (2018) 729–748, https://doi.org/10.5194/wes-2017-62.
[4] J. Carroll, A. McDonald, D. McMillan, Failure rate, repair time and unscheduled O&M cost analysis of offshore wind turbines, Wind energy. 2016;19(6) (2016) 1107–1119, https://doi.org/10.1002/we.1887.
[5] K. Kishinami, H. Taniguchi, J. Suzuki, H. Ibano, T. Kazunou, M. Turuhami, Theoretical and experimental study on the aerodynamic characteristics of a horizontal axis wind turbine, Energy 30 (11–12) (2005) 2089–2100, https://doi.org/10.1016/j.energy.2004.08.015.
[6] R. Jain, R. Kasturi, B.G. Schunck, Machine vision, McGraw-hill, New York, 1995.
[7] R. Jayakumar, B. Suresh, A review on edge detection methods and techniques, International Journal of Advanced Research in Computer and Communication Engineering 3 (4) (2014) 6369–6371.
[8] S. Savant, A review on edge detection techniques for image segmentation, International Journal of Computer Science and Information Technologies 5 (4) (2014) 5898–5900.
[9] M. Mukherjee, Y. U. Potdar, and A. U. Potdar, Object tracking using edge detection. In Proceedings of the International Conference and Workshop on Emerging Trends in Technology, New York, United States, (2010), pp. 686-689. 10.1145/1741906.1742064.
[10] S.J. Laurence, On tracking the motion of rigid bodies through edge detection and least-squares fitting, Experiments in Fluids. 52 (2) (2012) 387–401, https://doi.org/10.1007/s00348-011-1228-6.
[11] Z. Li, G. Zhao, S. Li, H. Sun, R. Tao, X. Huang, Y.J. Guo, Rotation feature extraction for moving targets based on temporal differencing and image edge detection, IEEE Geoscience and remote sensing letters 13 (10) (2016) 1512–1516, https://doi.org/10.1109/LGRS.2016.2594299.
[12] L. Zhao, Q. Zhao, H. Liu, P. Lv, D. Gu, Structural sparse representation-based semi-supervised learning and edge detection proposal for visual tracking, Visual Computer 33 (9) (2017) 1169–1184, https://doi.org/10.1007/s00371-016-1279-z.
[13] X. Bai, M. Yang, B. Ajmera, An advanced edge-detection method for noncontact structural displacement monitoring, Sensors 20 (17) (2020) 4941, https://doi.org/10.3390/s20174941.
[14] A.P. Daga, L. Garibaldi, GA-adaptive template matching for offline shape motion tracking based on edge detection: IAS estimation from the SURVISHNO 2019 challenge video for machine diagnostics purposes, Algorithms 13 (2) (2020) 33, https://doi.org/10.3390/a13020033.
[15] J.R. Bell, S.J. Rothberg, Laser vibrometers and contacting transducers, target rotation and six degree-of-freedom vibration: what do we really measure? Journal of Sound and Vibration 237 (2000) 245–261, https://doi.org/10.1006/jsvi.2000.3053.
[16] S. Rothberg, M. Allen, P. Castellini, An international review of laser Doppler vibrometry: making light work of vibration measurement, Optics and Lasers in Engineering. 99 (1) (2017) 11–22, https://doi.org/10.1016/j.optlaseng.2016.10.023.
[17] P. Sriram, S. Hanagud, J. Craig, N.M. Komerath, Scanning laser Doppler technique for velocity profile sensing on a moving surface, Applied Optics 29 (16) (1990) 2409–2417, https://doi.org/10.1364/AO.29.002409.
[18] P. Sriram, S. Hanagud, J. Craig, Mode shape measurement using a scanning laser Doppler vibrometer, The International Journal of Analytical and Experimental Modal, Analysis 7 (3) (1992) 169–178.
[19] M.S. Allen, M.W. Sracic, A new method for processing impact excited continuous-scan laser Doppler vibrometer measurements, Mechanical Systems and Signal Processing 24 (3) (2010) 721–735, https://doi.org/10.1016/j.ymssp.2009.11.004.
[20] D.M. Chen, Y.F. Xu, W.D. Zhu, Damage identification of beams using a continuously scanning laser Doppler vibrometer system, Journal of Vibration and Acoustics 138 (5) (2016) 05011, https://doi.org/10.1115/1.4033639.
[21] S. Yang, M.S. Allen, Lifting approach to simplify output-only continuous-scan laser vibrometry, Mechanical Systems and Signal Processing 45 (2) (2014) 267–282, https://doi.org/10.1016/j.ymssp.2013.11.010.
[22] Y.F. Xu, D.M. Chen, W.D. Zhu, Operational modal analysis using lifted continuously scanning laser Doppler vibrometer measurements and its application to baseline-free structural damage identification, Journal of Vibration and Control 25 (7) (2019) 1341–1364, https://doi.org/10.1177/1077546318821154.
[23] A. Stanbridge, D. Ewins, Modal testing using a scanning laser Doppler vibrometer, Mechanical Systems and Signal Processing 13 (2) (1999) 255–270, https://doi.org/10.1006/mssp.1998.1209.
[24] D. Di Maio, D. Ewins, Continuous scan, a method for performing modal testing using meaningful measurement parameters, Part I, Mechanical Systems and Signal Processing 25 (8) (2011) 3027–3042, https://doi.org/10.1016/j.ymssp.2011.05.018.
[25] D.M. Chen, Y.F. Xu, W.D. Zhu, Experimental investigation of notch-type damage identification with a curvature-based method by using a continuously scanning laser Doppler vibrometer system, Journal of Nondestructive Evaluation 36 (2) (2017) 38, https://doi.org/10.1007/s10921-017-0418-4.
[26] Y.F. Xu, D.M. Chen, W.D. Zhu, Damage identification of beam structures using free response shapes obtained by use of a continuously scanning laser Doppler vibrometer system, Mechanical Systems and Signal Processing 92 (2017) 226–247, https://doi.org/10.1016/j.ymssp.2016.12.042.
[27] Y.F. Xu, D.M. Chen, W.D. Zhu, Modal parameter estimation using free response measured by a continuously scanning laser Doppler vibrometer system with application to structural damage identification, Journal of Sound and Vibration 485 (2020), 115536, https://doi.org/10.1016/j.jsv.2020.115536.
[28] A. Stanbridge, D. Ewins, A. Khan, Modal testing using impact excitation and a scanning LDV, Shock and Vibration 7 (2) (2000) 91–100, https://doi.org/10.1155/2000/527389.
[29] K. Yuan, W.D. Zhu, Estimation of modal parameters of a beam under random excitation using a novel 3D continuously scanning laser Doppler vibrometer system and an extended demodulation method, Mechanical Systems and Signal Processing 155 (2021), 107606, https://doi.org/10.1016/j.ymssp.2021.107606.
[30] C. Ao, B. Qiao, L. Chen, J. Xu, M. Liu, X. Chen, Blade dynamic strain non-intrusive measurement using L1/2-norm regularization and transmissibility, Measurement 190 (2022), 110677, https://doi.org/10.1016/j.measurement.2021.110677.
[31] C. Ao, B. Qiao, M. Liu, W. Zhu, Y. Zhu, Y. Wang, X. Chen, Non-contact full-field dynamic strain reconstruction of rotating blades under multi-mode vibration, Mechanical Systems and Signal Processing 186 (2023), 109840, https://doi.org/10.1016/j.ymssp.2022.109840.
[32] D.M. Chen, Y.F. Xu, W.D. Zhu, Identification of damage in plates using full-field measurement with a continuously scanning laser Doppler vibrometer system, Journal of Sound and Vibration 422 (2018) 542–567, https://doi.org/10.1016/j.jsv.2018.01.005.
[33] D. Chen, Y.F. Xu, W.D. Zhu, Non-model-based identification of delamination in laminated composite plates using a continuously scanning laser Doppler vibrometer system, Journal of Vibration and Acoustics 140 (4) (2018), 041001, https://doi.org/10.1115/1.4038734.

[34] D.M. Chen, Y.F. Xu, W.D. Zhu, A comprehensive study on detection of hidden delamination damage in a composite plate using curvatures of operating deflection shapes, Journal of Nondestructive Evaluation 38 (2019) 54, https://doi.org/10.1007/s10921-019-0591-8.
[35] A.B. Stanbridge, M. Martarelli, D.J. Ewins, Rotating disc vibration analysis with a circular-scanning LDV, in Proceedings of IMAC XIX, Orlando, USA, 2001, pp. 1211–1217.
[36] I. Bucher, P. Schmiechen, D.A. Robb, D.J. Ewins, Laser-based measurement system for measuring the vibration on rotating discs, First International Conference on Vibration Measurements by Laser Techniques: Advances and Applications, Ancona, Italy 2358 (1994) 398–408, https://doi.org/10.1117/12.185355.
[37] P. Castellini, F. Giovanucci, G. Nava-Mambretti, L. Scalise, E.P. Tomasini, Vibration analysis of tyre treads: a in-plane laser vibrometry approach, In Society for Experimental Mechanics Inc, 16th International Modal Analysis Conference, Ancona, Italy 2 (1998) 1732–1738.
[38] A. Fioretti, D. Di Maio, D.J. Ewins, P. Castellini, E.P. Tomasini, Deflection shape reconstructions of a rotating five-blade helicopter rotor from TLDV measurements, AIP Conference Proceedings, Ancona, Italy 1253 (1) (2010) 17–28, https://doi.org/10.1063/1.3455457.
[39] D. Di Maio, D.J. Ewins, Applications of continuous tracking SLDV measurement methods to axially symmetric rotating structures using different excitation methods, Mechanical Systems and Signal Processing 24 (8) (2010) 3013–3036, https://doi.org/10.1016/j.ymssp.2010.06.012.
[40] A. Gasparoni, M.S. Allen, S. Yang, M.W. Sracic, P. Castellini, E.P. Tomasini, Experimental modal analysis on a rotating fan using tracking-CSLDV, AIP Conference Proceedings, Ancona, Italy 1253 (1) (2010) 3–16, https://doi.org/10.1063/1.3455482.
[41] M. Martarelli, P. Castellini, C. Santolini, E.P. Tomasini, Laser Doppler vibrometry on rotating structures in coast-down: resonance frequencies and operational deflection shape characterization, Measurement Science and Technology 22 (11) (2011), 115106, https://doi.org/10.1088/0957-0233/22/11/115106.
[42] H. Khalil, D. Kim, J. Nam and K. Park, Operational deflection shape of rotating object using tracking laser Doppler vibrometer, in 2015 IEEE International Conference on Electronics, Circuits, and Systems, Cairo, Egypt, (2015), pp. 693-696. 10.1109/ICECS.2015.7440411.
[43] B.J. Halkon, S.R. Frizzel, S.J. Rothberg, Vibration measurements using continuous scanning laser vibrometry: velocity sensitivity model experimental validation, Measurement Science and Technology 14 (6) (2003) 773, https://doi.org/10.1088/0957-0233/14/6/310.
[44] B.J. Halkon, S.J. Rothberg, Vibration measurements using continuous scanning laser Doppler vibrometry: theoretical velocity sensitivity analysis with applications, Measurement Science and Technology 14 (3) (2003) 382, https://doi.org/10.1088/0957-0233/14/3/318.
[45] B.J. Halkon, S.J. Rothberg, Vibration measurements using continuous scanning laser vibrometry: advanced aspects in rotor applications, Mechanical Systems and Signal Processing 20 (6) (2006) 1286–1299, https://doi.org/10.1016/j.ymssp.2005.11.009.
[46] P. Castellini, E.P. Tomasini, Image-based tracking laser Doppler vibrometer, Review of Scientific Instruments 75 (1) (2004) 222–232, https://doi.org/10.1063/1.1630859.
[47] L.F., Lyu, and W.D. Zhu,, Operational modal analysis of a rotating structure under ambient excitation using a tracking continuously scanning laser Doppler vibrometer system, Mechanical Systems and Signal Processing 152 (2021), 107367, https://doi.org/10.1016/j.ymssp.2020.107367.
[48] L.F., Lyu, and W.D. Zhu,, Operational modal analysis of a rotating structure subject to random excitation using a tracking continuously scanning laser Doppler vibrometer via an improved demodulation method, Journal of Vibration and Acoustics 144 (1) (2021), 011006, https://doi.org/10.1115/1.4051178.
[49] L.F. Lyu, W.D. Zhu, Full-field mode shape estimation of a rotating structure subject to random excitation using a tracking continuously scanning laser Doppler vibrometer via a two-dimensional scan scheme, Mechanical Systems and Signal Processing 169 (2022), 108532, https://doi.org/10.1016/j.ymssp.2021.108532.
[50] L.F. Lyu, G.D. Higgins, W.D. Zhu, Operational modal analysis of a rotating structure using image-based tracking continuously scanning laser Doppler vibrometry via a novel edge detection method, Journal of Sound and Vibration 525 (2022), 116797, https://doi.org/10.1016/j.jsv.2022.116797.
[51] R. Wiser, M. Bolinger, B. Hoen, D. Millstein, J. Rand, G. Barbose, B. Paulos, Land-based wind market report: 2022 edition., Lawrence Berkeley National Lab, Berkeley, CA (United States) (2022), https://doi.org/10.2172/1882594.
[52] A. Dräbenstedt, J. Sauer, C. Rembe, Remote-sensing vibrometry at 1550 nm wavelength, In AIP Conference Proceedings 1457 (1) (2012) 113–121, https://doi.org/10.1063/1.4730549.
[53] G.D. Acar, B.F. Feeny, Bend-bend-twist vibrations of a wind turbine blade, Wind Energy 21 (1) (2018) 15–28, https://doi.org/10.1002/we.2141.
[54] Y. Chen, A.S.E. Mendoza, D.T. and Griffith,, Experimental and numerical study of high-order complex curvature mode shape and mode coupling on a three-bladed wind turbine assembly, Mechanical Systems and Signal Processing 160 (2021), 107873, https://doi.org/10.1016/j.ymssp.2021.107873.
[55] K. Yuan, W.D. Zhu, Estimation of modal parameters of a beam under random excitation using a novel 3D continuously scanning laser Doppler vibrometer system and an extended demodulation method, Mechanical Systems and Signal Processing 155 (2021), 107606, https://doi.org/10.1016/j.ymssp.2021.107606.